nature materials

ARTICLES

PUBLISHED ONLINE: 30 JANUARY 2017 | DOI: 10.1038/NMAT4848

Endocytic reawakening of motility in jammed epithelia

Chiara Malinverno[1†], Salvatore Corallino[1†], Fabio Giavazzi[2*], Martin Bergert[3], Qingsen Li[1], Marco Leoni[4], Andrea Disanza[1], Emanuela Frittoli[1], Amanda Oldani[1], Emanuele Martini[1], Tobias Lendenmann[3], Gianluca Deflorian[1], Galina V. Beznoussenko[1], Dimos Poulikakos[3], Kok Haur Ong[5], Marina Uroz[6,7,8,9], Xavier Trepat[6,7,8,9], Dario Parazzoli[1], Paolo Maiuri[1], Weimiao Yu[5], Aldo Ferrari[3*], Roberto Cerbino[2*] and Giorgio Scita[1,10*]

Dynamics of epithelial monolayers has recently been interpreted in terms of a jamming or rigidity transition. How cells control such phase transitions is, however, unknown. Here we show that RAB5A, a key endocytic protein, is sufficient to induce large-scale, coordinated motility over tens of cells, and ballistic motion in otherwise kinetically arrested monolayers. This is linked to increased traction forces and to the extension of cell protrusions, which align with local velocity. Molecularly, impairing endocytosis, macropinocytosis or increasing fluid efflux abrogates RAB5A-induced collective motility. A simple model based on mechanical junctional tension and an active cell reorientation mechanism for the velocity of self-propelled cells identifies regimes of monolayer dynamics that explain endocytic reawakening of locomotion in terms of a combination of large-scale directed migration and local unjamming. These changes in multicellular dynamics enable collectives to migrate under physical constraints and may be exploited by tumours for interstitial dissemination.

Collective cell migration is essential for tissue morphogenesis during development and repair, and also for tumour dissemination[1]. Most aspects of multicellular migration are ruled by the physical interactions that cells establish among each other and with their environment. For example, during collective migration within confluent monolayers, cell sheets flow like a fluid yet remain fixed and solid-like at short timescales, with the motion of each cell constrained by the cell crowding due to its neighbours[2–4]. As cell density rises, neighbouring cells restrict the motion of each cell, forcing them to move in groups, surprisingly similar to what is observed in systems of inert particles that undergo a jamming or rigidity transition at large density[4–7]. However, while the transition in inert systems invariably occurs at a critical particle packing ϕ_c (ref. 8), epithelial monolayers display limited density fluctuations. Therefore, material parameters that encode cell properties such as cell–cell adhesion and cortical tension, rather than density alone, have been proposed to govern the rigidity transition in cell monolayers[5,6,9–11]. However, the general validity of this theoretical framework remains to be investigated. Even less understood are the molecular determinants and cellular processes that regulate multicellular dynamics by impacting on physical properties.

A cellular process that influences cellular and multicellular motility strategies is membrane trafficking[12,13]. Here, we report that perturbation of endocytosis by altering the levels of its master regulator RAB5A[14,15] is sufficient to reawaken the motility of jammed epithelial monolayers. RAB5A causes large, anisotropic and spatially correlated motility streams by globally enhancing endosomal trafficking and macropinocytic internalization. These variations impact on junctional tension, topology and dynamics of junctional proteins, facilitating coherent cell motion over long distances. RAB5A further promotes the extension of protrusions aligned to the local velocity of migratory cohorts. RAB5A-induced reawakening of motility is associated with a growing length scale, precluding an understanding of monolayer dynamics simply in terms of an increase in local rearrangements. A self-propelled Voronoi model that includes an active cell reorientation mechanism accounts for RAB5A-induced multicellular dynamics. The model identifies a motility regime that we define as flowing liquid, where local and long-range collective motility coexist. As a consequence of these emerging material properties, RAB5A monolayers are not only efficient in directed locomotion during wound closure or epiboly gastrulation movement in zebrafish development, but also display a high degree of plasticity that allows them to migrate under physical constraints typical of interstitial tissues architecture. These properties may be exploited in tumorigenic settings to escape the intrinsic motility-suppressive environment of jammed epithelial tissues.

Results

RAB5A promotes coherent and ballistic collective motility. To test the role of endocytic trafficking on collective epithelial locomotion, we perturbed the levels of RAB5A by generating doxycycline-inducible, RAB5A-expressing populations of human

[1]IFOM-FIRC Institute of Molecular Oncology, Via Adamello, 16, 20139 Milan, Italy. [2]Università degli Studi di Milano, Dipartimento di Biotecnologie Mediche e Medicina Traslazionale, I-20090 Segrate, Italy. [3]ETH Zurich, Laboratory of Thermodynamics in Emerging Technologies, Sonneggstrasse 3, 8092 Zurich, Switzerland. [4]Institut Curie, 26 rue d'Ulm 75248 Paris Cedex 05, France. [5]Institute of Molecular and Cell Biology (IMCB), A(*)STAR, Singapore 138673, Singapore. [6]Institute for Bioengineering of Catalonia, Barcelona, Barcelona 08028, Spain. [7]Catalan Institution for Research and Advanced Studies (ICREA), 08010 Barcelona, Spain. [8]CIBER de Bioingeniería, Biomateriales y Nanomedicina (CIBER-BBN), 28029 Madrid, Spain. [9]Facultat de Medicina, Universitat de Barcelona, 08036 Barcelona, Spain. [10]Università degli Studi di Milano, Dipartimento di Oncologia e Emato-Oncologia, I-20133 Milan, Italy. [†]These authors contributed equally to this work.
*e-mail: fabio.giavazzi@unimi.it; aferrari@ethz.ch; Roberto.Cerbino@unimi.it; Giorgio.Scita@ifom.eu

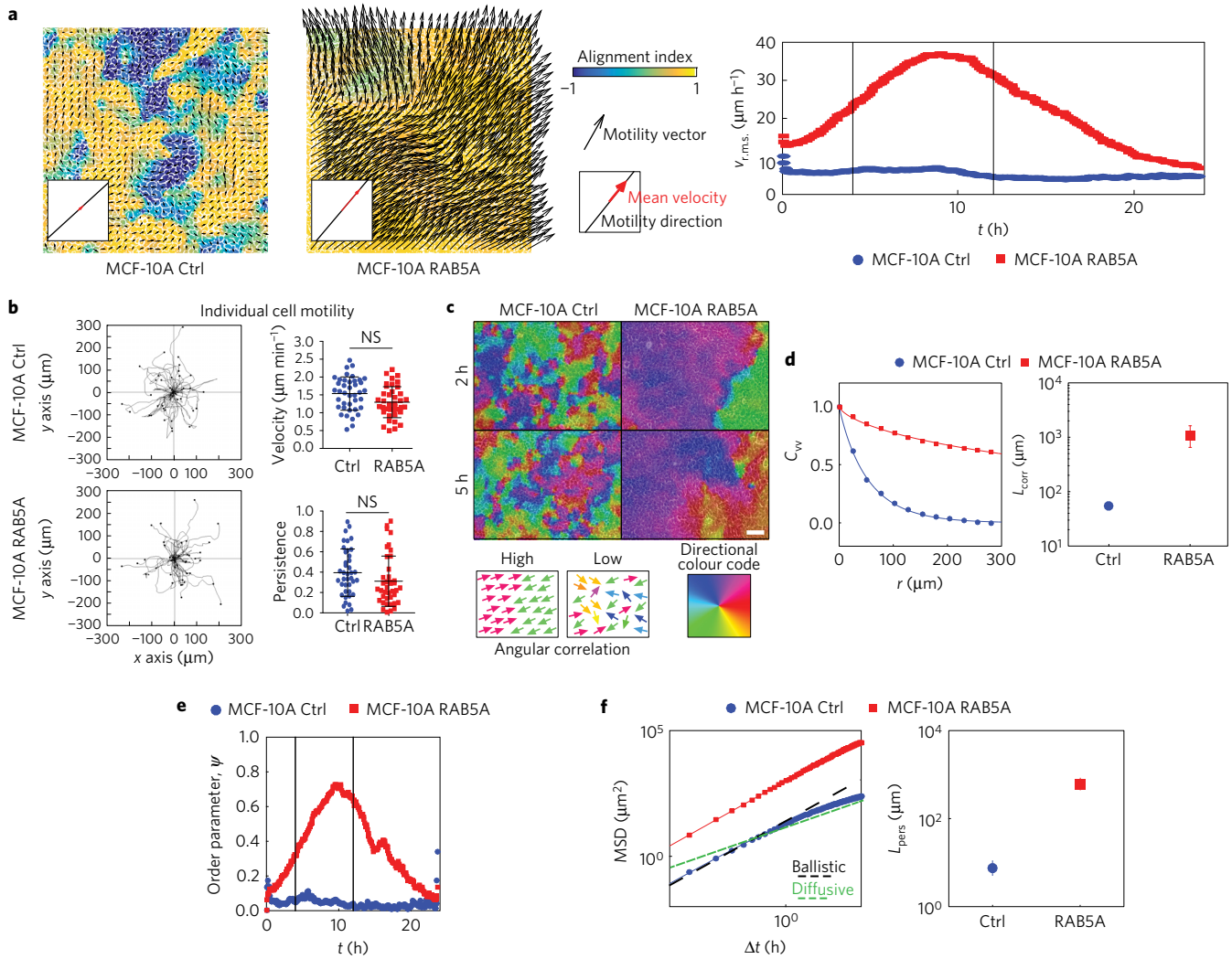

Figure 1 | RAB5A promotes coherent, ballistic motion of jammed epithelia. a, Left: snapshots of the velocity field obtained from PIV analysis of doxycycline-treated control (Ctrl) and RAB5A-MCF-10A cells seeded at jamming density and monitored by time-lapse microscopy (Supplementary Movie 2). The red arrow in each inset is the mean velocity $\mathbf{v}_0$ (average over the entire field of view). The colour map reflects the alignment with respect to the mean velocity, quantified by the parameter $a(x) = (\mathbf{v}(x) \cdot \mathbf{v}_0)/(|\mathbf{v}(x)||\mathbf{v}_0|)$. The local velocity is parallel ($a = +1$) or antiparallel ($a = -1$) to the mean direction of migration. Right: root mean square velocity $v_{r.m.s.}$ (representative of >10 independent experiments). Vertical lines indicate the time interval used for the analysis of motility parameters. **b**, Left plots: migration paths of control and RAB5A-MCF-10A cells (Supplementary Movie 6) seeded sparsely to monitor individual cell motility and analysed using the Chemotaxis Tool ImageJ software plugin. Right plots: velocity and persistence of the locomotion of cells. Data are the mean ± s.d. ($n = 40$ single cells/experiment/genotype of three independent experiments); NS, not significant. **c**, Snapshots depicting the angular velocity of control and RAB5A-MCF-10A cells seeded at jamming density and monitored by time-lapse microscopy (Supplementary Movie 7). Angular velocity vectors are calculated by CIV analysis. The colour code indicates the direction of migration. Homogeneous and inhomogeneous scattered colours indicate regions with high and low migration coherence, respectively. Scale bar, 100 μm. Representative images from $n = 5$ time-lapse series. **d**–**f**, PIV analysis of motion of doxycycline-treated control and RAB5A-MCF-10A cells seeded at jamming density (Supplementary Movie 2). In **e**, vertical lines indicate the time interval used for the analysis of motility parameters. **d**, Left: velocity correlation functions C_{VV} evaluated in the time window comprised between 4 and 12 h during which the availability of EGF allows migration. The continuous lines are best fits of C_{VV} with a stretched exponential function. Right: correlation lengths L_{corr} (five movies/experimental condition out of three to eight independent experiments). **e**, Order parameter ψ as a function of time. $\psi = 1$ means a perfectly uniform velocity field. $\psi \cong 0$ indicates randomly oriented velocities. **f**, Left: mean square displacements (MSD) obtained by numerical integration of the velocity maps. Right: persistence length L_{pers} obtained by fitting the MSD curves with a model function (continuous lines) describing the transition from a short-time ballistic to a long-time diffusive behaviour.

mammary epithelial MCF-10A cells (Supplementary Fig. 1a). These cells form polarized monolayers and, upon reaching confluence, display a typical collective locomotion mode characterized by the emergence of large-scale, coordinated motility streams, involving tens of cells. As cells keep on dividing, density increases, causing a near complete kinetic arrest akin to a jamming or rigidity transition[5,16] (Supplementary Fig. 1b and Supplementary Movie 1). Unexpectedly, under these latter conditions, elevation of RAB5A-reawakened motility of kinetically arrested monolayer by promoting large and heterogeneous multicellular streams (Fig. 1a and Supplementary Movies 2 and 3). RAB5A expression had marginal effects on the rate of cell division of confluent monolayers (Supplementary Fig. 1c), and collective motility was unperturbed by inhibition of cell division (Supplementary Fig. 1d and Supplementary Movie 4). Large-scale, collective locomotion was also induced by expression of RAB5A in jammed keratinocyte monolayers (Supplementary Fig. 1e and Supplementary Movie 5) and oncogenically transformed

MCF-10A variants, MCF10DCIS.com (not shown). Finally, RAB5A expression did not alter the migration of individual MCF-10A cells in random migration assays (Fig. 1b and Supplementary Movie 6). Thus, RAB5A effects on motility are emergent properties of cell collectives that elicit reawakening of locomotion of kinetically arrested, jammed epithelia.

Collective locomotion depends on complex cell–cell interactions and communication occurring during the migration of epithelial sheets[17]. To characterize the phenotype induced by RAB5A in MCF-10A cells, we analysed movies by cell image velocimetry (CIV)[18] and particle image velocimetry (PIV)[19], focusing on the time window where the full availability of soluble epidermal growth factor (EGF) enables locomotion (see Methods). We found that RAB5A expression robustly enhances cell coordination (Fig. 1c and Supplementary Movie 7). A simple indicator of the collective nature of cell motion is obtained by calculating the velocity correlation length L_{corr} as the width of the correlation function $C_{VV}(\mathbf{r}) = (\langle \mathbf{v}(\mathbf{x}_0 + \mathbf{r}) \cdot \mathbf{v}(\mathbf{x}_0) \rangle) / \langle |\mathbf{v}(\mathbf{x}_0)|^2 \rangle$ of the (vectorial) velocity $\mathbf{v}(\mathbf{x}_0)$ (see Methods). We observe a 20-fold increase of L_{corr} from $55 \pm 5\,\mu m$ (control) to $1.1 \pm 0.3\,mm$ (RAB5A), which corresponds to about 50 cell diameters (Fig. 1d and Supplementary Movie 2). The directionality of collective motion is captured well by the order parameter ψ (see Methods), which can vary in the range [0 to 1]: $\psi = 1$ corresponds to a perfectly uniform velocity field, where all the cells move in the same direction and with the same speed, while $\psi \cong 0$ is expected for a randomly oriented velocity field. While for the control ψ always remains below 0.1, we observed a marked increase in ψ for the RAB5A monolayer (Fig. 1e), in correspondence with a substantial increase of absolute motility, quantified by the root mean square velocity $v_{r.m.s.} = \sqrt{\langle |\mathbf{v}|^2 \rangle}$ (Fig. 1a). We also quantified cellular motions using their mean square displacement (MSD) over a given time interval, Δt. For both control and RAB5A, the MSD exhibits for short times a quadratic scaling with Δt: MSD $\cong (u_0 \Delta t)^2$, which is indicative of a directed ballistic motion, although with dramatically different characteristic velocities ($u_0 = 32\,\mu m\,h^{-1}$ for RAB5A, $u_0 = 6\,\mu m\,h^{-1}$ for the control). At later times, a transition to a diffusive-like regime characterized by a scaling exponent close to 1 is observed (Fig. 1f). An estimate of the persistence length L_{pers}, corresponding to the typical distance travelled by a cell with constant velocity before the direction of its motion becomes randomized, gives L_{pers} less than one cell diameter for control cells, while for RAB5A $L_{pers} = 650\,\mu m$, corresponding to more than 30 cell diameters (Fig. 1f).

RAB5A alters junctional mechanics and monolayers rigidity. Cell–cell coordination during collective locomotion is influenced by the strength and dynamics of cell–cell adhesion. We hypothesize that RAB5A may impinge on these junctional processes.

We initially investigated the distribution of the junctional marker E-cadherin. Our results showed that junctions of control cells were rather wavy. Conversely, RAB5A cells displayed straight and compact junctions (Fig. 2a,b), and increased surface contact area (Fig. 2b). P-cadherin and the tight junctional markers ZO-1 also display similar RAB5A-induced topological alterations (Supplementary Fig. 2a). Thus, RAB5A might globally increase cell surface contacts and tension. Frequently, indeed, the straightening of junctions correlates with an increase in junctional strength and tension[20]. Consistently, instantaneous recoil of cadherin clusters from the cut site (caused by two-photon laser nano-scissors) indicated that RAB5A expression increased local junctional tension similar to that observed after hypotonic stimulation, used as control[21] (Fig. 2c and Supplementary Movie 8). RAB5A had no impact on actomyosin contractility measured by determining the levels of phosphorylated myosin light chains (Fig. 2b), albeit RAB5A-induced motility was sensitive to blebbistatin (Supplementary Fig. 2c). Instead, RAB5A was found, by atomic force microscopy, to increase the overall monolayer rigidity to levels comparable to those obtained by hypotonic stimulation on control cells (Fig. 2d).

Increased endomembrane trafficking promotes motility. RAB5 is a master regulator of endocytic processes[22]. We therefore assessed whether elevation of RAB5A in MCF-10A enhances these processes globally and whether their perturbation, in turn, prevents RAB5A-induced reawakening of motility.

RAB5A expression increased, as expected, the size and the number of EEA-1-positive early endosomes (Supplementary Fig. 3a). Using fluorescence recovery after photobleaching (FRAP) experiments, we further showed that RAB5A increases the mobility of membrane cargo, and most notably of GFP-E-cadherin (Fig. 3a), whose turnover is primarily mediated by endo/exocytic trafficking[23] (Fig. 3a and Supplementary Movie 9). Furthermore, blockade of endocytosis by pharmacological inhibition of the pinchase dynamin with Dynasore[24] impaired E-cadherin internalization (Supplementary Fig. 3b) and severely reduced velocity correlation, persistence length, and ballistic motility (Fig. 3b and Supplementary Movie 10).

RAB5 is also essential to control dynamin-independent internalization processes, including the intake of large macromolecules and fluids, through phagocytosis[25] and macropinocytosis[26]. Consistently, elevation of RAB5A increased the intake of high-molecular weight dextran, used to track macropinocytosis (Supplementary Fig. 3c). This process was impaired by treatment with EIPA [5-(N-Ethyl-N-isopropyl)amiloride], an inhibitor of Na+/H+ exchangers that blocks macropinocytosis[27] (Supplementary Fig. 3c). Remarkably, EIPA abrogated RAB5A-dependent collective locomotion and robustly decreased the mean velocity and velocity correlation length (Fig. 3c and Supplementary Movie 11).

Endocytic perturbations, besides affecting intracellular trafficking, may also alter fluid intake and membrane homeostasis, ultimately impacting on junctional topology and dynamics. If this scenario is correct, then altering these processes through alternative biophysical interventions might be sufficient to instigate collective locomotion and mimic the phenotype induced by RAB5A. To this end, we exposed monolayers to hypo- and hypertonic media. Remarkably, hypotonic treatment of control, jammed monolayers was sufficient to straighten junctions (Supplementary Fig. 4a), reawakened cell motility and increased velocity correlation and persistence length (Fig. 3d and Supplementary Movie 12). Conversely, the exposure to hypertonic media abrogated RAB5A-collective locomotion, which was, instead, enhanced by hypotonic stimulation (Fig. 3e and Supplementary Movie 13).

Thus, one mechanism through which RAB5A acts is by promoting global alterations in endocytic processes. These changes may, in turn, be critical to increase junctional tension and dynamics, and monolayer rigidity to promote RAB5A-induced long-range motility. Fluctuations in fluid intake and membrane tension may also be important here. However, hypotonic treatment reawakened the motility of jammed epithelia only 6–10 h after the initial treatment (Fig. 3d and Supplementary Movie 12). Thus, changes in water influx, volume and membrane tension, which are rapid (within seconds or minutes) cell responses[28], are unlikely to account for the effects on monolayer kinematics. Conversely, long exposure to hypotonic stimulation augmented internalization and turnover rate of E-cadherin (Supplementary Fig. 4b,c), endosome size[21], and junctional topology (Supplementary Fig. 4a) and tension (Fig. 2c), mimicking the effects of RAB5A and indicating that global perturbation of endocytosis drives collective locomotion.

RAB5A induces polarized cell protrusions and traction forces. One striking feature of RAB5A-induced large-scale streaming flows is their persistent and ballistic motility, suggesting that individual cells must efficiently orient their motion with the local direction

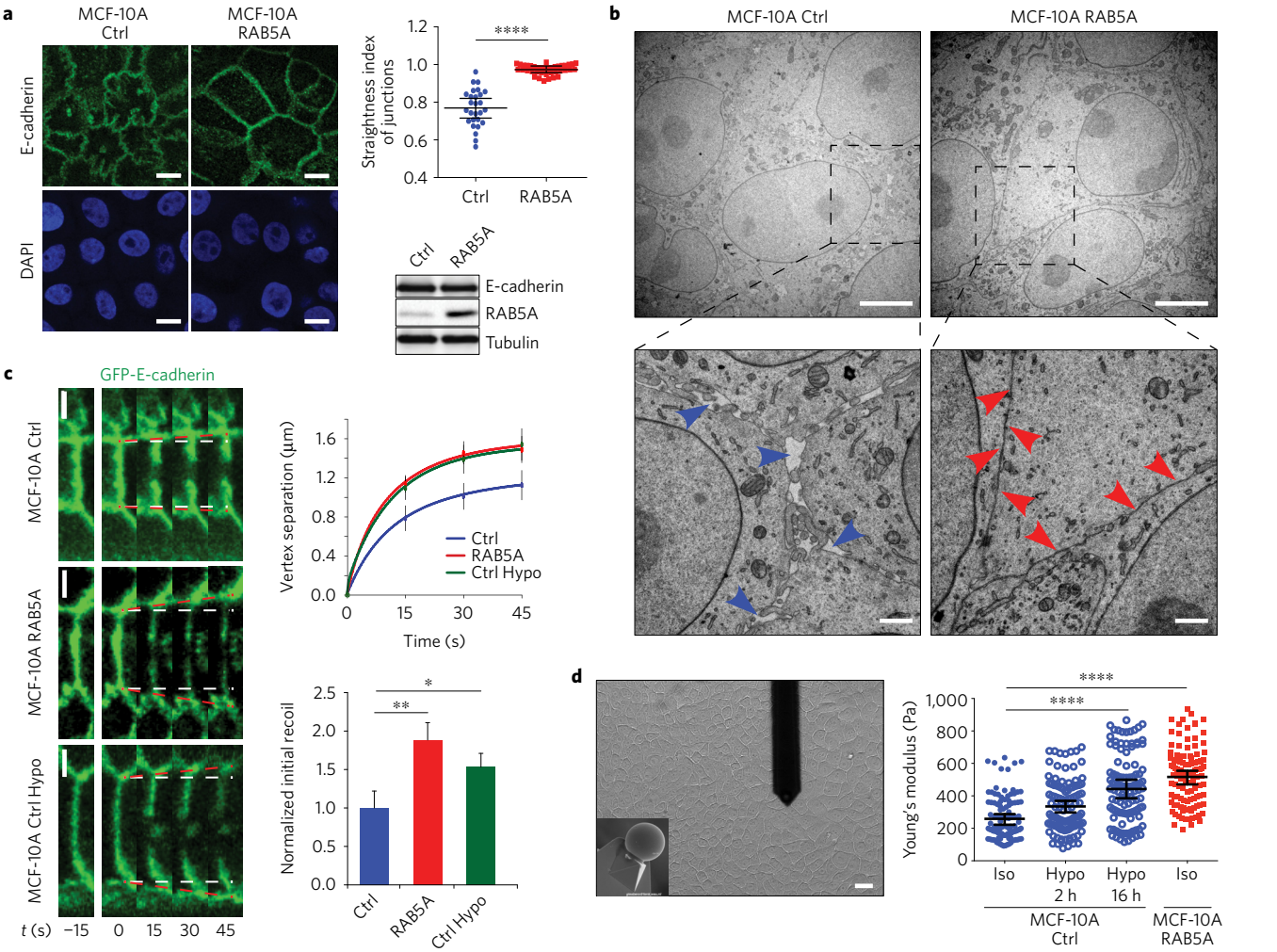

Figure 2 | RAB5A alters junctional topology, tension and monolayer rigidity. a, Left images: confocal apical sections of fully confluent and jammed control and RAB5A-MCF-10A monolayers, stained for E-cadherin (green) and DAPI (blue). Scale bars, 10 μm. Top right plot: the straightness index of junctions was quantified as the ratio of the distance between vertices and the junctional length. Data are the mean ± standard error of the mean (s.e.m.) ($n = 80$ cells in three independent experiments/condition). $^{****}p < 0.0001$. Bottom right: E-cadherin total levels detected by immunoblotting analysis of lysates of control and RAB5A cells. Tubulin was used as loading control. **b**, Representative electron microscopy micrographs of fully confluent control and RAB5A-MCF-10A monolayers (scale bars, 5 μm). Boxes indicate magnified areas shown in the bottom images (scale bars, 1 μm). Blue arrows point to large spaces between cell–cell contacts, red arrows to tight cell–cell contacts. **c**, Left images: image sequence of GFP-E-cadherin-positive junctional vertices recoiling after nano-scissor laser ablation at $t = 0$ in control (MCF-10A Ctrl) and RAB5A-MCF-10A cells. GFP-E-cadherin-expressing cells (MCF-10A Ctrl Hypo) incubated with hypotonic buffer were used as positive control. Recoiling vertices were measured as a proxy of junctional tension. White dashed lines indicate starting positions of vertices; red dotted lines indicate expansion of vertices after laser ablation. Top right graph: Initial recoil was measured by the instantaneous rate of vertex separation at $t = 0$, and computed using best-fit single-exponential curves. Bottom right plot: Initial recoil rate was normalized with respect to control cells. Data are the means ± s.d., normalized to control. ($n = 20$, 19 and 17 for control, RAB5A and hypo cells, respectively). Scale bars, 5 μm. $^{**}p < 0.001$; $^{*}p < 0.05$. **d**, Left: representative snapshot of the cantilever touching a MCF-10A monolayer and bottom view of the microsphere (10 μm in diameter) probe of the cantilever (inset). Scale bar, 20 μm. Right: Young's modulus of control and RAB5A-MCF-10A monolayers seeded at jamming density obtained by atomic force microscopy (AFM) indentation. Control monolayers were incubated either in isotonic or hypotonic buffers. The position of the AFM indentation was chosen to be the centre of the cell. Young's modulus was calculated using the Hertz model. Data are the mean ± s.e.m. ($n = 80$ cells/condition of three independent experiments). $^{****}p < 0.0001$.

of migration. Actin-based, polarized protrusions are a proxy of cell-oriented locomotion. In monolayers, these protrusions extend underneath neighbouring cells and are called cryptic lamellipodia. By monitoring the dynamics of EGFP-LifeAct-expressing cells interspersed with non-fluorescent cells (Fig. 4a,b), we detected, only in RAB5A monolayers, the formation of cryptic lamellipodia oriented along the motility direction of supracellular motility streams (Fig. 4b and Supplementary Movie 14). RAB5A-induced cryptic lamellipodia are RAC1-dependent, consistent with the role of RAB5A endo/exocytic cycles in spatially restricting RAC1 signalling for protrusions extension[29]. Indeed, a pharmacological inhibitor of RAC1 activation reduced cryptic lamellipodia formation (Fig. 4c and Supplementary Movie 15), and impaired the motility of RAB5A monolayers (Fig. 4d and Supplementary Movie 16).

These findings indicate that RAB5A monolayers might exert large traction forces on the substrate during locomotion. To directly assess this possibility, we measured surface tractions of control and RAB5A monolayers using a novel confocal reference-free traction force microscopy (cTFM)[30]. We found that RAB5A monolayers exert significantly higher and more dynamic substrate tractions (Fig. 4e and Supplementary Fig. 5a) that moved with the flow

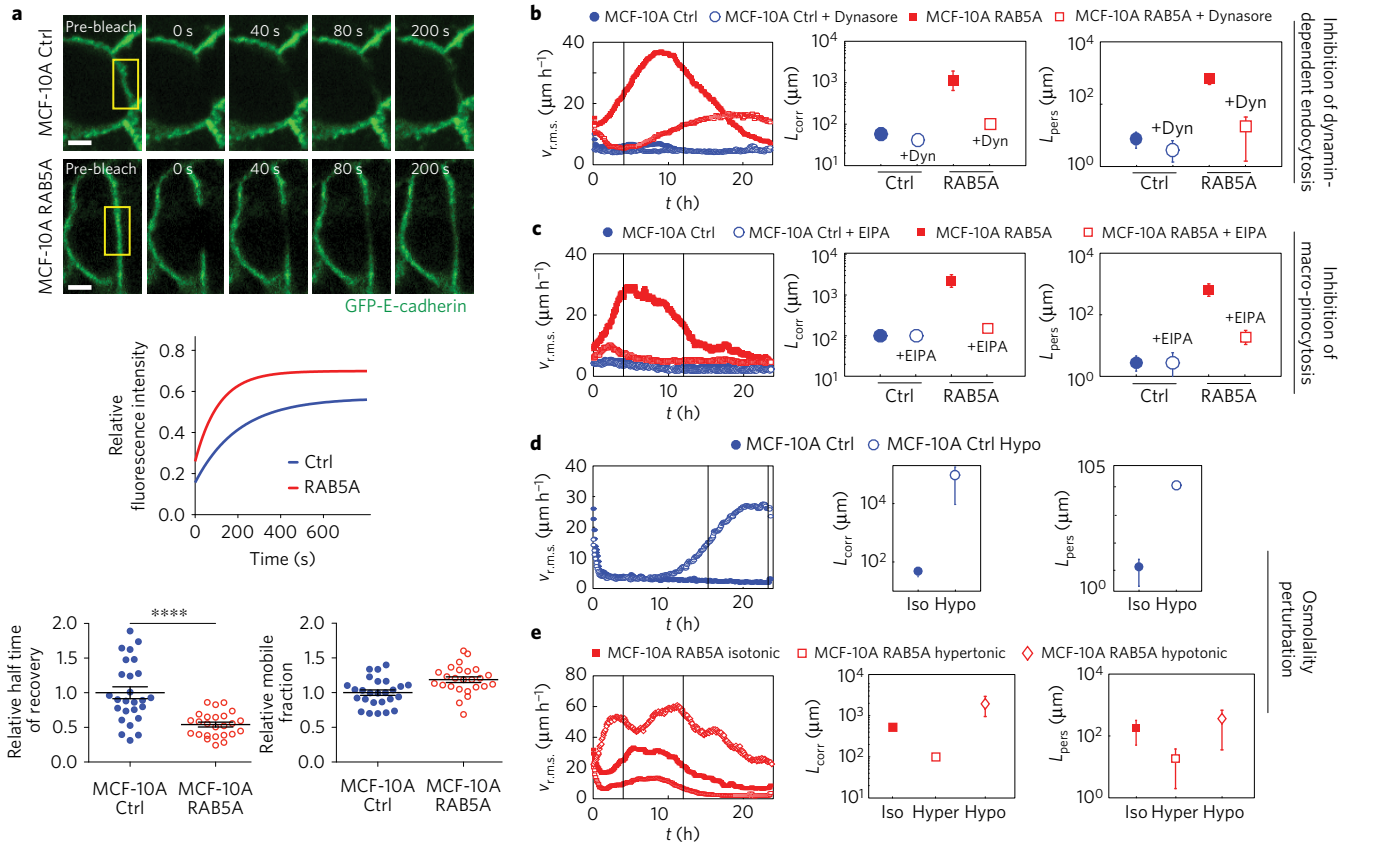

Figure 3 | Endomembrane trafficking mediates RAB5A-induced collective motility. a, Top images: Series of images depicting fluorescence recovery after photobleaching (FRAP) of GFP-E-cadherin in the outlined region of interest (yellow box) in fully confluent control and RAB5A-MCF-10A cells (Supplementary Movie 9). Scale bars, 5 μm. Middle graph: representative single-exponential best-fit curves of fluorescence recovery. Bottom plots: the halftime of recovery (left) and mobile fraction (right) were calculated from the best-fit curves and are expressed as mean ± s.d. ($n = 30$ cells/condition of one representative experiment out of three with identical outcome). ****$p < 0.0001$, calculated with paired Student's t-test. **b**, Dynamin-dependent inhibition of endocytosis impairs RAB5A-induced collective motility. Doxycycline-treated control and RAB5A-MCF-10A monolayers seeded at jamming density were incubated with vehicle or Dynasore (Dyn) 1 h before starting time-lapse recording (Supplementary Movie 10). PIV analysis was applied to extract (from left to right): root mean square velocity $v_{r.m.s.}$ plotted as a function of time; correlation lengths L_{corr} and persistence lengths L_{pers}. **c**, Macropinocytosis inhibition impairs RAB5A-induced collective motility. Doxycycline-treated control and RAB5A-MCF-10A monolayers seeded at jamming were incubated with EIPA [5-(N-Ethyl-N-isopropyl)amiloride] (75 μM) 1 h before starting time-lapse recording (Supplementary Movie 11). From left to right: root mean square velocity $v_{r.m.s.}$ plotted as a function of time; correlation lengths L_{corr} and persistence lengths L_{pers} obtained from PIV analysis. **d**–**e**, Hypotonic treatment causes MCF-10A monolayer unjamming, while hypertonic stimulation blocks RAB5A-induced collective motility. **d**, Jammed control MCF-10A monolayers were treated with hypotonic media before recording their motility (Supplementary Movie 12). From left to right: temporal evolution of the mean square velocity $v_{r.m.s.}$, velocity correlation lengths L_{corr} and persistence lengths L_{pers} obtained by PIV analysis. **e**, Doxycycline-treated RAB5A monolayers seeded at a jamming density were incubated with either hypotonic or hypertonic media before recording their motility (Supplementary Movie 13). From left to right: temporal evolution of the mean square velocity $v_{r.m.s.}$, velocity correlation lengths L_{corr} and persistence lengths L_{pers} obtained by PIV analysis. For all PIV experiments, at least five movies/experimental condition were analysed in three to ten independent experiments. In **b**–**e**, vertical lines indicate the time interval used for the analysis of motility parameters.

tracking velocity fields (Supplementary Movie 17). We obtained higher traction forces of RAB5A than control monolayers also by measuring the displacements of fluorescent beads embedded into polyacrylamide gel substrates[31] (Supplementary Fig. 5b,c).

Thus, RAB5A promotes the extension of aligned cell protrusions in combination with increased and more dynamic substrate tractions, both of which combine to promote monolayer unjamming and collective motility.

Endocytosis controls a flowing liquid mode of motility. Our data suggest that RAB5A-induced reawakening is the result of a complex interplay between changes in cell adhesion and cortical tension, which are both altered in RAB5A monolayers as a consequence of changes in endomembrane dynamics (Figs 2 and 3). This is accompanied by the efficient alignment of cell protrusions and dynamic tractions to ignite multicellular directed migration (Fig. 4).

To elucidate how these different contributions combine in our experiments, we performed numerical simulations of monolayer dynamics. Our simulations are based on a self-propelled Voronoi (SPV) model with few basic ingredients. The first is a target shape index p_0 that is the result of the competition between intracellular adhesion and cortical tension, recently introduced in the context of a vertex model[6]. The latter model was found to describe well the unjamming of bronchial epithelial layers[5] even in the absence of intrinsic cell motility mechanisms. The second ingredient is a prescribed self-propulsive speed for each cell, as also proposed in a recent SPV model[32]. At variance with the latter model, where the cell polarity is described as a unit vector undergoing random rotational diffusion, we assume a Vicsek-like polar alignment mechanism between the polarization direction of neighbouring cells[2]. The alignment efficiency depends on the characteristic response time τ that each cell takes to actively align its polarity along the direction

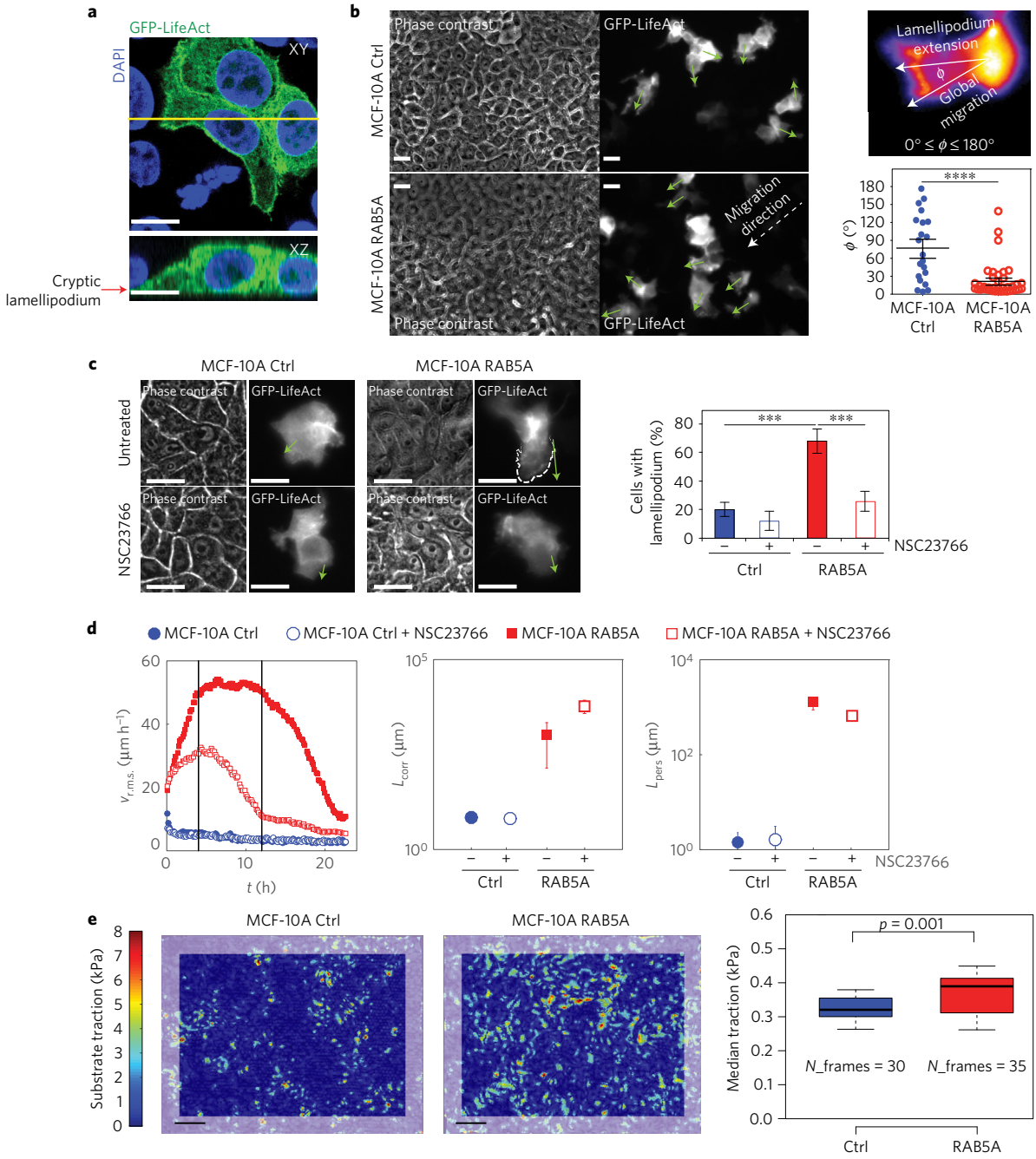

Figure 4 | RAB5A promotes polarized cell protrusions and traction forces. a, Mixed (1:10 ratio) GFP-LifeAct-expressing (green): non-expressing control MCF-10A cells were processed for epifluorescence or stained with DAPI (Blue). Arrow points to a cryptic lamellipodium. The yellow line indicates the region of *XY* projection shown in the *XZ* plane in the bottom image. Scale bars, 15 μm. **b**, Left images: still phase-contrast and fluorescent images of the extension and orientation of cryptic lamellipodia in unwounded control and RAB5A-MCF-10A monolayers composed of mixed (1:10 ratio) GFP-LifeAct-expressing (green):non-expressing cells monitored by time-lapse microscopy (Supplementary Movie 14). Green arrows indicate the orientations of protrusions. Scale bars, 15 μm. Top right image: representation of the angle Φ between the direction of each lamellipodium and the direction vector of a moving collective pack (group migration); $\Phi \sim 0°$ indicates that protrusions and group migration have the same direction; $\Phi > 80°$ indicates that the directions of protrusions and group migration are diverging. Bottom right plot: quantification of the orientation angle Φ ($n = 25$/condition from five independent experiments). Data are the mean ± s.e.m. $^{****}p < 0.0001$. **c**, Left images: phase contrast and fluorescent still images depicting cryptic lamellipodia in untreated and NCS23766 (a RAC1 inhibitor)-treated unwounded control and RAB5A monolayers composed of GFP-LifeAct-expressing (green) and non-expressing cells seeded at a 1:10 ratio and monitored by time-lapse fluorescence microscopy (Supplementary Movie 15). Green arrows indicate the orientation of a typical protrusion. Scale bars, 15 μm. Right plot: proportion of cells with lamellipodium. Data are the mean ± s.d. ($n = 80$ cell/condition in three independent experiments). $^{***}p < 0.0005$. **d**, From left to right: temporal evolution of the root mean square velocity $v_{r.m.s.}$, velocity correlation lengths L_{corr} and persistence lengths L_{pers} calculated by PIV analysis of control and RAB5A-MCF-10A monolayers seeded at jamming density and treated with the RAC1 inhibitor NSC23766 or vehicle and monitored by time-lapse phase-contrast microscopy (Supplementary Movie 16). At least five movies/experimental condition were analysed in three independent experiments. **e**, Left images: substrate tractions of control and RAB5A monolayers measured using cTFM[30]. Grey frames correspond to areas excluded from analysis due to boundary effects. Scale bars, 25 μm. Right plot: the median traction analysed from *n* time points, obtained from five to six fields of view out of two independent experiments. *p*-value calculated with Mann–Whitney-U-Test.

of its local velocity (Supplementary Fig. 8 in Supplementary Information, section Computational Model). A study of the phase diagram reveals four different regimes for the monolayer dynamics (Fig. 5a). When the response time τ is large, the system behaviour is mainly controlled by the target shape index p_0 (refs 5,32): for small values of p_0, the monolayer is jammed; by contrast, for increasing p_0, cell adhesion favours local cell rearrangements leading to unjamming, as previously described[5]. Changes in index p_0 reflect monotonically on the average shape parameter q, defined as the ratio between cell perimeter and square root of the cell area. Jamming occurs when $q = q^* = 3.81$ (refs 5,32).

If the response time τ is decreased in the presence of a non-negligible single-cell speed, large-scale collective motility is observed in simulations that can be identified either as a flowing solid (for small p_0, large correlation length in the absence of local cell rearrangements) or a flowing liquid (large p_0, large correlation length in the presence of local cell rearrangements). The latter case, in which both local and collective motility are present, captures RAB5A phenotypes (Fig. 5b and Supplementary Movie 18). A slow, short-range correlated rearrangement dynamics without directed motion (Fig. 5c and Supplementary Movie 18) is instead compatible with the non-flowing liquid-like state of control monolayers. Our simulations suggest that RAB5A acts mainly to decrease the response time τ, in agreement with the increased protrusive activity and more efficient stress transmission detected in our experiments.

Next, we verified experimentally a key topological feature of our model and use it to produce testable predictions. We first compared the time dependence of the shape parameter q during reawakening of cell motility induced by RAB5A (Supplementary Movie 3). Notably, while q remains almost constant in time for the control, it increases in RAB5A monolayers during the first stages of reawakening (Fig. 5d,e), indicating that the shape parameter is the control parameter of the jamming transition also in the presence of self-propulsion and reorientation.

In light of this, the observed increase of q should also lead to a topological unjamming. To test this prediction, we compared the self-overlap order parameter Q and the four-point susceptibility χ_4 (Methods and ref. 5) of control and RAB5A monolayers. This comparison was performed by first removing the average displacement due to collective directed locomotion, when present (see Methods for details), which is instead captured by the order parameter ψ (Fig. 5f). Results showed that while control cells simply slow down in time, the local dynamics in RAB5A monolayers is characterized by faster rearrangements accompanied by a decreasing length scale of dynamic heterogeneities (Fig. 5g–j).

Biological consequences of endocytic reawakening of motility. RAB5A-increase in monolayer motility predicts that deregulation of this protein may also influence the plastic motility behaviour of collective entities. We tested this prediction on directional migration in wound repair processes, migration into confined spaces, and on gastrula morphogenesis in zebrafish. Firstly, RAB5A monolayers closed a wound two times faster than control cells (Fig. 6a and Supplementary Movie 19), whereas silencing of RAB5 genes impaired wound closure speed (Fig. 6a and Supplementary Movie 19). CIV analysis revealed that RAB5A enhanced angular velocity correlation length (Supplementary Fig. 6a and Supplementary Movie 20), consistent with the increased cell coordination observed in unwounded monolayers (Fig. 1c–e). RAB5A accelerated wound closure also of oncogenic MCF10DCIS.com cells[33], and of immortalized HaCaT keratinocytes (Supplementary Fig. 6b,c). Higher-magnification analysis of the wound-front cells further revealed that RAB5A monolayers extended larger and more persistent protrusions than control cells (Fig. 6b and Supplementary Movie 21). We also detected cryptic lamellipodia coherently oriented toward the wound in RAB5A, but not in control cells located more than ten cell rows behind the leading edge (Supplementary Fig. 6d and Supplementary Movie 22). We exploited these features to estimate indirectly the experimental orientational response time τ, which our numerical simulations predict to be significantly shorter for RAB5A cells. Firstly, we noticed that RAB5A monolayers are significantly faster in reaching maximum speed soon after wounding and in reorienting their angular velocity (Supplementary Fig. 7a). Secondly, kymograph analysis of wounded monolayers revealed that RAB5A cells move into the wound as highly correlated sheets with a directed velocity that remains constant even 40–50 cells away from the wound edge (Supplementary Fig. 7b). Thus, RAB5A cells are more efficient in long-range propagation of stresses and have reduced random rotational motion (noise) that leads to a reduction of reorientation time τ.

A multicellular tissue that has gained fluid-like properties might be optimally fitted to flows into confined channels, mimicking those encountered by normal and tumour cells disseminating into interstitial tissues[34]. To this end, we performed two-dimensional migration assays of mammary monolayers using micro-fabricated polydimethylsiloxane (PDMS) channels of 25 μm width, which mimic the space between collagen interfaces observed *in vivo*[34]. Both control and RAB5A-MCF-10A monolayers crossed these channels, moving in a collective fashion. However, RAB5A monolayers efficiently flowed, like streams, into these narrow slits, resulting in a much higher number of cells crossing the paths (Fig. 6c and Supplementary Movie 23).

The gastrulating embryo is an additional, striking example of directed, collective migration[35]. Gastrulation is initiated by spreading of meso- and endodermal (mesendodermal) cell sheets over the yolk cells, a process called epiboly. Epiboly is governed by the strength of cell–cell adhesion mediated by E-cadherin molecules and requires RAB5-dependent endosomal trafficking of this molecule[36,37]. We therefore assessed whether ectopic expression of mammalian RAB5A accelerates epiboly. We injected one-cell-stage wild-type zebrafish embryos with control or human CFP-RAB5A mRNA and monitored epiboly progress between 3 and 8 h post fertilization. Epifluorescence analysis revealed that CFP-hRAB5A was readily expressed (Fig. 6d) and robustly accelerated the epiboly progress (Fig. 6d and Supplementary Movie 24).

Conclusions

We found that RAB5A controls a diverse set of collective motility processes *in vitro* and *in vivo* by re-awaking the directional, coordinated locomotion of jammed and kinetically arrested monolayers. RAB5A exerts this function by promoting the formation of polarized, actin-based, lamellipodia that generate traction forces, which can be efficiently transmitted at long ranges through enhanced junctional contact and stresses. The increased mechanical coupling also enables a cell to obtain directional guidance cues from their neighbours, forcing adjacent cells to align their front-rear polarity, resulting in a positive feedback between polarity and net displacement. This, combined with increased dynamic of junctional E-cadherin to accommodate for cell neighbouring exchange, volume, density and strain fluctuations, collaboratively enable multicellular entities to acquire a fluid-like character. These alterations appear primarily to be the results of mechanical changes caused by global membrane trafficking perturbations. However, given the inextricable link between endocytosis and signalling, we cannot exclude that amplification and rewiring of specific biochemical pathways, particularly those emanating from EGF receptors, underpins some of the altered mechanical properties—a possibility that is currently under investigation. Importantly, these changes of plasticity promote the motility of otherwise jammed and glassy-like monolayers, leading to invasive, collective migration under physical confinement and accelerated multicellular directed migration during embryonic development.

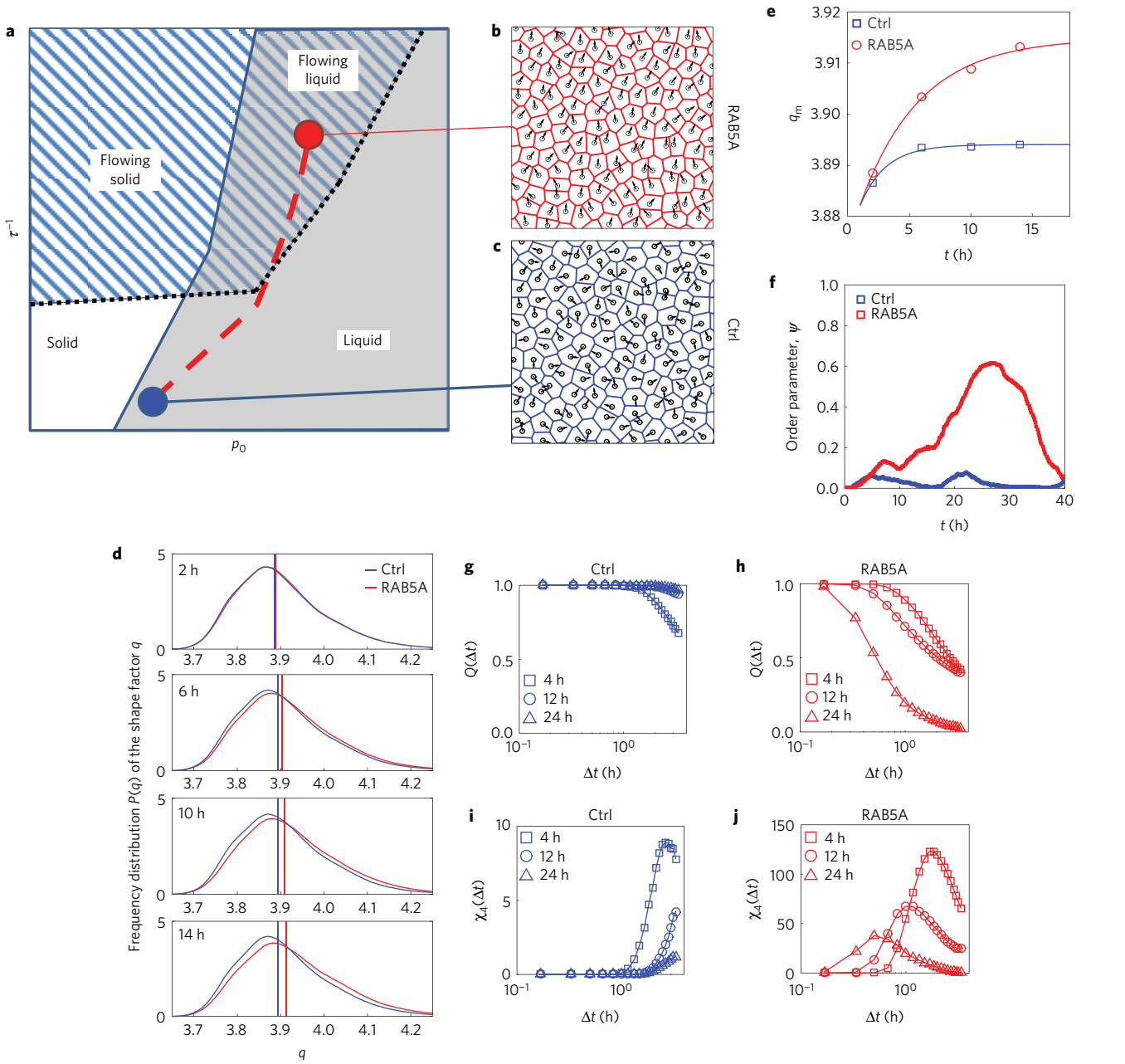

Figure 5 | RAB5A induces a collective flowing liquid mode of locomotion. a, Qualitative phase diagram obtained from simulations. Control parameters are the target shape index p_0, encoding the effective junctional line tension, and the inverse reorientation time τ^{-1}, expressing the efficiency of the local alignment of self-propelled cell velocities. Two transition lines are present. The first one (continuous blue line) separates the solid (jammed, no mutual rearrangements of the cells) phase from the liquid phase. This transition is governed by the average shape parameter q, which attains the critical value of $q^* = 3.81$ across the transition. A second (dotted black) line separates a flowing phase, where directed collective migration is observed and the order parameter ψ is non-zero, and a non-flowing phase, where no long-range orientational order is present. The dashed red line is a schematic representation of the trajectory in the phase space corresponding to the RAB5A-induced reawakening. **b**, Representative snapshot of the simulated monolayer in a flowing liquid state, where both directed collective migration is present and cell rearrangements are allowed (Supplementary Movie 18, right). **c**, Representative snapshot of the simulated monolayer in a non-flowing state, close to the solid–liquid transition (Supplementary Movie 18, left). **d**, Distributions of the experimentally determined shape parameter q at different stages during the reawakening experiment for Ctrl (blue curves) and RAB5A (red curves). Each curve is obtained from statistics on $>10^4$ cells, followed over a time window of 3 h width and centred, from top to bottom, at 2, 6, 10, 14 h after the beginning of the experiment. Vertical lines represent the median value of the corresponding distribution. **e**, Median value of the shape parameter q_m during the first stages of reawakening for Ctrl (blue squares) and RAB5A (red circles). **f**, Time evolution of order parameter ψ for Ctrl (blue) and RAB5A (red) during the reawakening experiment. **g**,**h**, Average overlap order parameter $Q(\Delta t)$ for Ctrl (**g**, blue) and RAB5A (**h**, red) at different stages during the reawakening experiment. Cells seeded at jamming density were treated with doxycycline. Movie recording started 4 h before addition of the drug. Each curve is obtained from reconstructed cell trajectories during a time window of 3 h and centred, respectively, around 4 (squares), 12 (circles) and 24 h (triangles) after the beginning of the experiment. The effect of collective sheet migration, when present, has been removed by correcting each cell trajectory for the average velocity of the monolayer, thus only mutual displacements contribute to $Q(\Delta t)$. **i**,**j**, Four-point susceptibility $\chi_4(\Delta t)$ for Ctrl (**i**, blue) and RAB5A (**j**, red symbols) at different stages during the reawakening experiment. Sampling intervals and symbols are as in **g**,**h**.

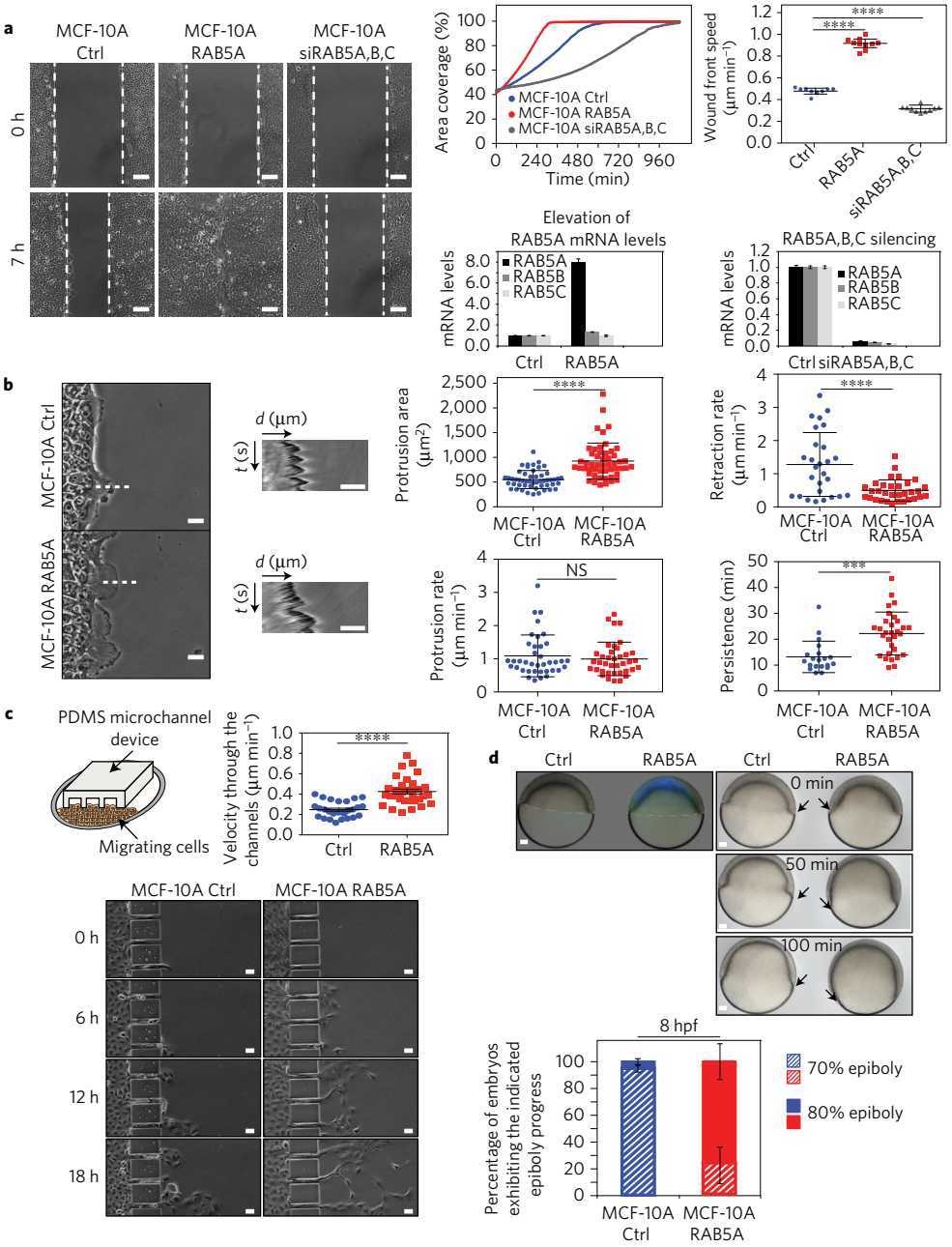

Figure 6 | Biological consequences of RAB5-induced flowing liquid mode of motion. a, Left images: scratched wound migration of doxycycline-treated control, RAB5A-MCF-10A, and RAB5A, B and C silenced monolayers (Supplementary Movie 19). Representative still images at the indicated time points are shown. Dashed lines mark the wound edges. Scale bars, 100 μm. Upper right graphs: motility was quantified by measuring (left) the percentage of area covered over time (calculations made with MatLab software) and (right) the wound-front mean speed. Data are the mean ± s.d. ($n = 20$ independent experiments). Bottom right graphs: the elevation of RAB5A mRNA (left) and the silencing of RAB5A, B and C (right) were verified by qRT-PCR (mRNA fold increase relative to the levels of control cells after normalizing for GAPDH mRNA levels). Data are the mean ± s.d. ($n = 20$ independent experiments). ****$p < 0.0001$. **b**, Left images: representative still images of the leading edge of wounded control and RAB5A-MCF-10A monolayers. Scale bars, 20 μm. Wound edge dynamics were monitored by time-lapse microscopy (images taken every 30 s, Supplementary Movie 21). Broken lines indicate areas used to perform kymograph analysis. Middle panels: kymographs of wound edge dynamics. Scale bars, 10 μm. Right plots: protrusion area, protrusion rate, retraction rates, and persistence were determined using the Kymograph ImageJ software plugin. Data are the mean ± s.d. ($n = 30$ kymograph lines/condition of five independent experiments). Protrusion area was measured manually using the ImageJ software. Data are the mean ± s.d. ($n = 30$/condition of four independent experiments). ***$p < 0.001$; ****$p < 0.0001$; NS, not significant. **c**, Top left panel: cartoon depicting the migration assay of MCF-10A monolayers moving into PDMS channels. Bottom images: still images of control and RAB5A-MCF-10A cells seeded as monolayers and entering into a micro-fabricated device with micro-channels of 25 μm width at the indicated time points. Scale bars, 25 μm. Top right plot: the velocity of cells passing through the channels was determined manually using the Chemotaxis Tool ImageJ software plugin. Data are the mean ± s.e.m.; ****$p < 0.001$. **d**, Top left image: lateral view of wild-type (WT) embryos injected with control or mRNA-encoding CFP-hRAB5A. Scale bar, 50 μm. Top right images: still images at the indicated time points of lateral views of control and CFP-hRAB5A-injected embryos during gastrulation. Arrows indicate mesendodermal cell fronts. Scale bars, 50 μm. Bottom plot: the fraction of embryos at the indicated percentage of epiboly progress was examined at 8 h post fertilization (hpf). Data are the mean ± s.d. ($n = 30$ embryos, two independent experiments).

Methods

Methods, including statements of data availability and any associated accession codes and references, are available in the online version of this paper.

Received 13 April 2016; accepted 15 December 2016; published online 30 January 2017

References

1. Friedl, P. & Gilmour, D. Collective cell migration in morphogenesis, regeneration and cancer. *Nat. Rev. Mol. Cell Biol.* **10,** 445–457 (2009).
2. Szabo, B. *et al*. Phase transition in the collective migration of tissue cells: experiment and model. *Phys. Rev. E* **74,** 061908 (2006).
3. Angelini, T. E., Hannezo, E., Trepat, X., Fredberg, J. J. & Weitz, D. A. Cell migration driven by cooperative substrate deformation patterns. *Phys. Rev. Lett.* **104,** 168104 (2010).
4. Angelini, T. E. *et al*. Glass-like dynamics of collective cell migration. *Proc. Natl Acad. Sci. USA* **108,** 4714–4719 (2011).
5. Park, J. A. *et al*. Unjamming and cell shape in the asthmatic airway epithelium. *Nat. Mater.* **14,** 1040–1048 (2015).
6. Bi, D., Lopez, J. H., Schwarz, J. M. & Manning, M. L. A density-independent rigidity transition in biological tissues. *Nat. Phys.* **11,** 1074–1079 (2015).
7. Sadati, M., Taheri Qazvini, N., Krishnan, R., Park, C. Y. & Fredberg, J. J. Collective migration and cell jamming. *Differentiation* **86,** 121–125 (2013).
8. Goodrich, C. P. *et al*. Jamming in finite systems: stability, anisotropy, fluctuations, and scaling. *Phys. Rev. E* **90,** 022138 (2014).
9. Zehnder, S. M., Suaris, M., Bellaire, M. M. & Angelini, T. E. Cell volume fluctuations in MDCK monolayers. *Biophys. J.* **108,** 247–250 (2015).
10. Marchetti, M. C. *et al*. Hydrodynamics of soft active matter. *Rev. Mod. Phys.* **85,** 1143–1189 (2013).
11. Zehnder, S. M. *et al*. Multicellular density fluctuations in epithelial monolayers. *Phys. Rev. E* **92,** 032729 (2015).
12. Sigismund, S. *et al*. Endocytosis and signaling: cell logistics shape the eukaryotic cell plan. *Physiol. Rev.* **92,** 273–366 (2012).
13. Corallino, S., Malabarba, M. G., Zobel, M., Di Fiore, P. P. & Scita, G. Epithelial-to-mesenchymal plasticity harnesses endocytic circuitries. *Front. Oncol.* **5,** 45 (2015).
14. Frittoli, E. *et al*. A RAB5/RAB4 recycling circuitry induces a proteolytic invasive program and promotes tumor dissemination. *J. Cell Biol.* **206,** 307–328 (2014).
15. Mendoza, P., Diaz, J., Silva, P. & Torres, V. A. Rab5 activation as a tumor cell migration switch. *Small GTPases* **5(1),** e28195 (2014).
16. Sadati, M., Nourhani, A., Fredberg, J. J. & Qazvini, N. T. Glass-like dynamics in the cell and in cellular collectives. *Wiley Interdiscip. Rev. Syst. Biol. Med.* **6,** 137–149 (2014).
17. Ng, M. R., Besser, A., Danuser, G. & Brugge, J. S. Substrate stiffness regulates cadherin-dependent collective migration through myosin-II contractility. *J. Cell Biol.* **199,** 545–563 (2012).
18. Milde, F. *et al*. Cell Image Velocimetry (CIV): boosting the automated quantification of cell migration in wound healing assays. *Integr. Biol.* (*Camb*) **4,** 1437–1447 (2012).
19. Petitjean, L. *et al*. Velocity fields in a collectively migrating epithelium. *Biophys. J.* **98,** 1790–1800 (2010).
20. Verma, S. *et al*. A WAVE2-Arp2/3 actin nucleator apparatus supports junctional tension at the epithelial zonula adherens. *Mol. Biol. Cell* **23,** 4601–4610 (2012).
21. Pietuch, A., Bruckner, B. R. & Janshoff, A. Membrane tension homeostasis of epithelial cells through surface area regulation in response to osmotic stress. *Biochim. Biophys. Acta* **1833,** 712–722 (2013).
22. Zeigerer, A. *et al*. Rab5 is necessary for the biogenesis of the endolysosomal system *in vivo*. *Nature* **485,** 465–470 (2012).
23. Borghi, N. *et al*. E-cadherin is under constitutive actomyosin-generated tension that is increased at cell–cell contacts upon externally applied stretch. *Proc. Natl Acad. Sci. USA* **109,** 12568–12573 (2012).
24. Macia, E. *et al*. Dynasore, a cell-permeable inhibitor of dynamin. *Dev. Cell* **10,** 839–850 (2006).
25. Kitano, M., Nakaya, M., Nakamura, T., Nagata, S. & Matsuda, M. Imaging of Rab5 activity identifies essential regulators for phagosome maturation. *Nature* **453,** 241–245 (2008).
26. Lanzetti, L., Palamidessi, A., Areces, L., Scita, G. & Di Fiore, P. P. Rab5 is a signalling GTPase involved in actin remodelling by receptor tyrosine kinases. *Nature* **429,** 309–314 (2004).
27. Masereel, B., Pochet, L. & Laeckmann, D. An overview of inhibitors of Na(+)/H(+) exchanger. *Eur. J. Med. Chem.* **38,** 547–554 (2003).
28. Gauthier, N. C., Masters, T. A. & Sheetz, M. P. Mechanical feedback between membrane tension and dynamics. *Trends Cell Biol.* **22,** 527–535 (2012).
29. Palamidessi, A. *et al*. Endocytic trafficking of Rac is required for the spatial restriction of signaling in cell migration. *Cell* **134,** 135–147 (2008).
30. Bergert, M. *et al*. Confocal reference free traction force microscopy. *Nat. Commun.* **7,** 12814 (2016).
31. Tambe, D. T. *et al*. Collective cell guidance by cooperative intercellular forces. *Nat. Mater.* **10,** 469–475 (2011).
32. Bi, D., Yang, X., Marchetti, M. C. & Manning, M. L. Motility-driven glass and jamming transitions in biological tissues. *Phys. Rev. X* **6,** 021011 (2016).
33. Miller, F. R., Santner, S. J., Tait, L. & Dawson, P. J. MCF10DCIS.com xenograft model of human comedo ductal carcinoma *in situ*. *J. Natl Canc. Inst.* **92,** 1185–1186 (2000).
34. Weigelin, B., Bakker, G.-J. & Friedl, P. Intravital third harmonic generation microscopy of collective melanoma cell invasion. *IntraVital* **1,** 32–43 (2012).
35. Warga, R. M. & Kimmel, C. B. Cell movements during epiboly and gastrulation in zebrafish. *Development* **108,** 569–580 (1990).
36. Song, S. *et al*. Pou5f1-dependent EGF expression controls E-cadherin endocytosis, cell adhesion, and zebrafish epiboly movements. *Dev. Cell* **24,** 486–501 (2013).
37. Arboleda-Estudillo, Y. *et al*. Movement directionality in collective migration of germ layer progenitors. *Curr. Biol.* **20,** 161–169 (2010).

Acknowledgements

Work is supported by grants from the following agencies: Associazione Italiana per la Ricerca sul Cancro (AIRC #10168 and #18621), MIUR (the Italian Ministry of University and Scientific Research), the Italian Ministry of Health, Ricerca Finalizzata (RF0235844), Worldwide Cancer Research (AICR-14-0335), and the European Research Council (Advanced-ERC-#268836) (to G.S.); the Italian Ministry of Education and Research, Futuro in Ricerca Project ANISOFT (RBFR125H0M) (to R.C. and F.G.); Spanish Ministry of Economy and Competitiveness (BFU2012-38146), the Generalitat de Catalunya (2014-SGR-927), and the European Research Council (StG-CoG-616480) (to X.T.). C.M. was supported by Fondazione Umberto Veronesi. S.C. was supported by an AIRC fellowship. M.B. and T.L. were supported by funding from ETH-grant ETH-12 15-1.

Author contributions

C.M. and S.C. designed and performed experiments, interpreted the data, and generated all the cell biological and molecular biological tools and reagents; F.G. analysed all time-lapse experiments, interpreted the data, and designed the computational model; M.B. and T.L. performed traction force microscopy experiments, and interpreted and analysed data; Q.L. designed and built micro-fabricated channels and performed AFM experiments; M.L. contributed to the development of the computational model and to its interpretation; A.D., A.O., E.M. and D.Parazzoli performed laser nano-scissor experiments of EGFP-E-cadherin and interpreted data migration data; E.F. performed immunofluorescence experiments; D.Poulikakos designed and interpreted CIV and cTFM experiments; K.H.O. and W.Y. executed the semi-automated tracking of cell shape and size; G.D. performed zebrafish experiments; G.V.B. performed electron microscopy analysis; M.U. performed traction force experiments, and interpreted and analysed data; X.T. designed traction force experiments, and helped developing the computational model and writing the paper; P.M. designed analytical tools, interpreted collective migration experiments and help in developing the computational model; A.F., R.C. and G.S. designed the research, analysed and interpreted the data and wrote the paper. Each author contributed to writing the paper.

Additional information

Supplementary information is available in the online version of the paper. Reprints and permissions information is available online at www.nature.com/reprints. Correspondence and requests for materials should be addressed to F.G., A.F., R.C. or G.S.

Competing financial interests

The authors declare no competing financial interests.

Methods

Cell cultures and transfection. MCF-10A cells were a kind gift of J. S. Brugge (Department of Cell Biology, Harvard Medical School, Boston, USA) and were maintained in Dulbecco's Modified Eagle Medium: Nutrient Mixture F-12 (DMEM/F12) medium (Invitrogen) supplemented with 5% horse serum, 0.5 mg ml^{-1} hydrocortisone, 100 ng ml^{-1} cholera toxin, 10 µg ml^{-1} insulin and 20 ng ml^{-1} EGF. MCF10DCIS.com cells were kindly provided by J. F. Marshall (Barts Cancer Institute, Queen Mary University of London, UK) and maintained in the same media of MCF-10A without cholera toxin. HaCat cells were purchased from CLS (#300493) and cultured in DMEM medium (Lonza) supplemented with 10% fetal bovine serum (FBS) and 4 mM L-Glutamine. All cell lines have been authenticated by cell fingerprinting and tested for mycoplasma contamination. Cells were grown at 37 °C in humidified atmosphere with 5% CO_2. MCF-10A, HaCat and MCF10DCIS.com cells were infected with pSLIK-neo-EV (empty vector control) or pSLIK-neo-RAB5A lentiviruses and selected with the appropriate antibiotic to obtain stable inducible cell lines. Constitutive expression of LifeAct-EGFP or EGFP-H2B was achieved by lentiviral and retroviral infection of MCF-10A cells with EGFP-LifeAct- puro or pBABE- puro-EGFP-H2B vectors, respectively.

Cell streaming and wound healing assays. Cells were seeded in six-well plates (1.5×10^6 cells/well) in complete medium and cultured until a uniform monolayer had formed. RAB5A expression was induced, where indicated, 16 h before performing the experiment by adding fresh complete media supplemented with 2.5 µg ml^{-1} doxycycline to cells. At the time of recording, fresh media containing EGF was added. The addition of 20 ng ml^{-1} of EGF is absolutely essential to enable cell locomotion. Consistently, the incubation of monolayers in the absence of EGF prevents the emergence of streaming motility (not shown). EGF-dependent, RAB5A-mediated reawakening of cell motility is invariably transient, occurring between 4 and 12 h after EGF addition, with a peak in velocity centred around 6–8 h. The subsequent velocity decay is probably caused by exhaustion of EGF. Comparable cell confluence was tested by differential interference contrast (DIC) imaging using a ×10 objective and counting the number of nuclei/field. In the cell streaming assay, the medium was refreshed before starting imaging. In wound healing assays, the cell monolayer was scratched with a pipette tip and carefully washed with 1× phosphate-buffered saline (PBS) to remove floating cells and create a cell-free wound area. The closure of the wound was monitored by time-lapse microscopy. An Olympus ScanR inverted microscope with ×10 objective was used to take pictures every 5–10 min over a 24–96 h period (as indicated in the figure legends). The assay was performed using an environmental microscope incubator set to 37 °C and 5% CO_2 perfusion. After cell induction, doxycycline was maintained in the media for the total duration of the time-lapse experiment. The percentage of area covered by cells (area coverage %) over time and wound-front speed were calculated with MatLab software. In the Mitomycin C experiment, 1 µg ml^{-1} inhibitor was added together with doxycycline in fresh media before starting imaging. For the wound healing assay performed on interfered cells, 2.5×10^5 cells/well were plated in a six-well plate and interfered the day after with 1 nM of siRNAs, following the same conditions already described in the RNA interference section in the Supplementary Information.

For plasma membrane tension perturbation by osmotic treatments, an equal volume of hypotonic buffer (H_2O + 1 mM $CaCl_2$ + 1 mM $MgCl_2$) or hypertonic buffer (complete growth medium + 200 mM sucrose-containing complete growth medium; final concentration 100 mM) was added to the cells.

For measurements of cryptic lamellipodia directionality, MCF-10A cells stably expressing EGFP-LifeAct were mixed in a 1:10 ratio with unlabelled cells and seeded in wound healing or cell streaming assays, as described before. Cell migration was monitored by time-lapse phase-contrast and fluorescence microscopy. In the wound healing assay, images were collected at multiple stage positions in each time loop, including at the leading edge of the migrating cell sheet and about ten cell rows behind the leading edge. Cryptic lamellipodia directionality was measured as the angle ϕ delimited by the direction of the single lamellipodium and the direction vector of locomotion of the collective pack: $\phi = 0°$ indicates that protrusions and group migration have the same direction; $\phi = 180°$ indicates that protrusions and group migration have opposite direction. Each assay was done five times and at least 25 cells/condition were counted in each experiment. Where indicated, Dynasore (80 µM), EIPA (75 µM), NSC23766 (100 µM) and Blebbistatin (25 µM) were added 1 or 2 h before imaging.

Kymograph analysis of cell protrusions. Wound healing assay was performed by Ibidi Culture Inserts (Ibidi) to avoid debrides affecting the quality of the kymograph analysis. Inserts were placed in a 12-well plates and MCF-10A cells were plated in each chamber, 5×10^4 cells/chamber. 16 h before starting the experiment, growing media was replaced with fresh complete media containing 2.5 µg ml^{-1} of doxycycline to induce RAB5A expression. A cell-free wound area was created by removal of the insert. Cell migration was monitored by an Olympus Scan^R inverted microscope with a ×20 objective (with an additional ×1.6 magnification lens).

Images from 10 positions/condition were recorded every 30 s over a 1 h period. To measure the dynamic of protrusive structures we used the Kymograph plugin of the ImageJ software. Dynamic parameters measured from kymograph images were persistence time (Δt), protrusion rate ($\Delta s1/\Delta t1$) and retraction rate ($\Delta s2/\Delta t2$). The same time interval and ROI length were set in the analysis of each condition.

Cell image velocimetry. Cell image velocimetry (CIV) analysis of monolayer and wound healing time series was performed as previously described[18,38]. Overlays of phase-contrast images and coloured migration direction were exported from the software. Uniform colour indicates a homogeneous migration direction, and thus high coherence between cells. Angular correlation during wound healing was quantified for each frame between cells at a distance of 100 µm.

Measurement of the cellular velocities and trajectories. Maps of the instantaneous cellular velocities were obtained by analysing time-lapse phase-contrast movies with a custom PIV software written in MatLab. The time interval between consecutive frames was 5 min or 10 min. The interrogation window was 32 × 32 pixels (pixel size 1.29 µm or 1.6 µm), with an overlap of 50% between adjacent windows. The number of cells comprised within one field of view (FOV) was typically 2500. For a given monolayer, time-lapse images from different (typically from five to ten) FOVs were simultaneously collected.

The instantaneous root mean square velocity $v_{\mathrm{r.m.s.}}(t)$ of a cell monolayer was computed as

$$v_{\mathrm{r.m.s.}}(t) = \sqrt{(1/M)\sum_{j=1}^{M}\langle|\mathbf{v}(t)|^2\rangle_j}$$

where $\langle|\mathbf{v}(t)|^2\rangle_j = (1/N)\sum_{n=1}^{N}|\mathbf{v}^{(j)}(\mathbf{x}_n,t)|^2$ is the mean square velocity within the jth FOV, $\mathbf{v}^{(j)}(\mathbf{x}_n,t)$ is the instantaneous velocity at the nth grid point $\mathbf{x}_n$ of the jth FOV, N is the number of grid points in one field of view and M is number of independent FOVs.

The instantaneous order parameter $\psi(t)$ of a cell monolayer was computed as $\psi(t) = (1/M)\sum_{j=1}^{M}(|\langle\mathbf{v}(t)\rangle_j|^2/\langle|\mathbf{v}(t)|^2\rangle_j)$, where M and $\langle|\mathbf{v}(t)|^2\rangle_j$ are defined as above, $\langle\mathbf{v}(t)\rangle_j = (1/N)\sum_{n=1}^{N}\mathbf{v}^{(j)}(\mathbf{x}_n,t)$ is mean vectorial velocity within the jth FOV and, as above, N is the number of grid points in one FOV. According to these definitions, we have $0 \le \psi(t) \le 1$. In particular, $\psi(t) = 1$ only if, within each FOV, the velocity field is perfectly uniform, that is, all the cells in the monolayer move with the same speed and in the same direction. Conversely, $\psi(t) \cong 0$ is expected for a randomly oriented velocity field.

The vectorial velocity correlation functions were calculated as $C_{\mathrm{VV}}(r) = (1/M)\sum_{j=1}^{M}(c_j/\langle|\mathbf{v}|^2\rangle_j)$, where c_j is the azimuthal and temporal average of the non-normalized velocity correlation function within the jth FOV, which is calculated as IDFT $\{|\mathrm{DFT}\{\mathbf{v}^{(j)}(\mathbf{x}_n,t)\}|^2\}$. Here DFT and IDFT are, respectively, the direct and inverse two-dimensional digital Fourier transforms. Unless otherwise stated in the main text, the temporal average was always performed over the time window comprised between 4 and 12 h from the beginning of the image acquisition. $\langle|\mathbf{v}|^2\rangle_j$ is the temporal average of the above defined $\langle|\mathbf{v}(t)|^2\rangle_j$ performed over the same time window.

To estimate the velocity correlation function L_{corr}, the velocity correlation functions $C_{\mathrm{VV}}(r)$ were fitted with a stretched exponential function of the form $f(r) = \mathrm{e}^{-(r/L_{\mathrm{corr}})^{\gamma}}$, where γ is a stretching exponent.

Cellular trajectories $\mathbf{r}_m(t)$ were calculated by numerical integration of the instantaneous velocity field as obtained from the PIV analysis (see ref. 3 and references therein). For each FOV a number of trajectories roughly corresponding to the number of cells were computed.

Mean squared displacements (MSDs) of the cells were calculated as $\mathrm{MSD}(\Delta t) = \langle|\boldsymbol{r}_m(t+\Delta t) - \boldsymbol{r}_m(t)|^2\rangle$, where the average was performed over all the trajectories and, unless otherwise stated in the main text, in the time window comprised between 4 and 12 h after the beginning of the experiment. This time window corresponds to the transient acquisition of cell locomotion induced by the addition of fresh EGF to the media just before the beginning of time-lapse recording. Within this time frame, the monolayer velocity peaks around 6–8 h, and subsequently decays, probably due to exhaustion of the motogenic factor. To estimate the persistence length L_{pers} of the cellular motion, the MSD curves were fitted with a function of the form $g(\Delta t) = (u_0\Delta t)^2/\left(1 + \left(u_0\Delta t/L_{\mathrm{pers}}\right)\right)$. This expression describes a transition between a short-time ballistic-like scaling $\mathrm{MSD}(\Delta t) \sim (u_0\Delta t)^2$, corresponding to rectilinear motion with a typical speed u_0, and a long-time scaling $\mathrm{MSD}(\Delta t) \sim \left(u_0 L_{\mathrm{pers}}\Delta t\right)$, corresponding to a diffusive-like behaviour with an effective diffusion coefficient $u_0 L_{\mathrm{pers}}/4$. Within this description the transition between the two regimes takes place for $\Delta t \approx 1/u_0 L_{\mathrm{pers}}$, that is, after the cell has travelled with an approximately constant velocity over a distance of approximately L_{pers}. The simple expression adopted for g captures the same short- and long-time asymptotic behaviours that are expected for a particle with non-negligible inertia performing a Brownian motion.

Traction force microscopy. Substrate tractions were measured using cTFM with an interdisc spacing of 3 μm (ref. 30). During the reference configuration reconstruction step, the position of the outermost quantum dot (QD) nanodiscs plus a region of 2 μm towards the inside was fixed. QD nanodiscs inside this fixed frame were then relaxed to original positions as described in ref. 30. As the fixed QD nanodiscs themselves are distorted, displacement reconstruction is prone to errors close to the image border. Therefore, final traction analysis was restricted to data originating from an area more than 15 μm from the image border.

Code availability. Custom MatLab code for wound healing analysis, particle image velocimetry (PIV) and cellular trajectory calculations is available from the corresponding author on request. Code for the numerical SPV-based modelling of monolayer kinematics is available from the corresponding author upon request, and a detailed description of the model and the related code will also be published elsewhere. Code for cell image velocimetry (CIV) and confocal traction force microscopy (cTMF) has been previously described and is available in refs 18,30, respectively.

Data availability. The authors declare that the data supporting the findings of this study are available within the paper and its Supplementary Information files.

References

38. Franco, D. *et al*. Accelerated endothelial wound healing on microstructured substrates under flow. *Biomaterials* **34,** 1488–1497 (2013).